

## Centrifugal Buoyancy Driven Turbulent Convection in a Thin Cylindrical Shell

Amirreza Rouhi<sup>1</sup>, Daniel Chung<sup>1</sup>, Ivan Marusic<sup>1</sup>, Detlef Lohse<sup>2,3</sup> and Chao Sun<sup>2,3</sup>

<sup>1</sup>Department of Mechanical Engineering  
 University of Melbourne, Victoria 3010, Australia

<sup>2</sup>Physics of Fluids Group and Max Planck Center for Complex Fluid Dynamics  
 MESA+ Institute and J. M. Burgers Centre for Fluid Dynamics  
 University of Twente, 7500 AE Enschede, The Netherlands

<sup>3</sup>Center for Combustion Energy, Key Laboratory for Thermal Science and Power Engineering of Ministry of Education  
 Department of Energy and Power Engineering, Tsinghua University, 100084 Beijing, China

### Abstract

Centrifugal buoyancy driven convection is closely related to Rayleigh–Bénard convection, and offers another approach to the ultimate regime of thermal convection. Here, we perform direct numerical simulations (DNSs) of centrifugal convection in a cylindrical shell rotating about its axis at constant angular velocity. The walls undergo solid-body rotation, and the flow is purely driven by the temperature difference between the cold inner wall and the hot outer wall. We invoke the thin-shell limit where radial variations in centrifugal acceleration can be neglected. The Prandtl number is 0.7 corresponding to air. For this setup we have two input parameters: 1) the Rayleigh number  $Ra$  characterising the driving by centrifugal (buoyancy) effect, and 2) the Rossby number  $Ro$  characterising the Coriolis effect. Here, we vary  $Ra$  from  $10^7$  to  $10^{10}$ , and the inverse Rossby number  $Ro^{-1}$  from 0 (no rotation) to 1. We find that the flow dynamics is subjected to an interplay between the driving buoyancy force and the stabilising Coriolis force, similar to that of Chong *et al.* (*Phys. Rev. Lett.*, vol. 119, 2017, 064501), but with an important difference owing to the different axis of rotation. Instead of the formation of highly coherent plume-like structures at optimal condition that maximises heat transport, here, the formation of strong bidirectional wind at optimal condition ( $Ro_{\text{opt}}^{-1} \approx 0.8$ ) minimises heat transport. By increasing  $Ra$  at  $Ro_{\text{opt}}^{-1}$ , the mean flow approaches the Prandtl–von Kármán (logarithmic) behaviour, yet full collapse on the logarithmic law is not reached at  $Ra = 10^{10}$ .

### Introduction

The ultimate regime of thermal convection remains difficult to observe, especially in Rayleigh–Bénard convection [1, 2] in which the flow is driven by heating from below and cooling from above. The ultimate regime occurs beyond a critical high Rayleigh number  $Ra^*$ , when the whole flow, including the thin boundary layers, become dominated by inertia [3, 4].  $Ra^*$  depends on Prandtl number  $Pr$ , domain of study (e.g. enclosed cylinder, enclosed box or periodic box), and domain aspect ratio. For instance, at Prandtl number  $Pr \approx 0.7 - 0.9$ , for cylindrical container with aspect ratios  $D/L = 0.5$  and  $1.0$  (where  $D$  and  $L$  are the cylinder diameter and height), the ultimate regime occurs beyond  $Ra^* \approx 10^{14}$  [5, 6]. In the ultimate regime both momentum and thermal boundary layers follow Prandtl–von Kármán (logarithmic) behaviour, and the effective heat-transfer scaling, encapsulated by the Nusselt number  $Nu$  to Rayleigh number  $Ra$  relationship, follows a steeper gradient (e.g.  $Nu \propto Ra^{0.38}$  [7]) compared to the classical regime ( $Ra < Ra^*$ ), where  $Nu \propto Ra^{0.31}$  [4].

To date, observing the logarithmic boundary layer in Rayleigh–Bénard convection, and consequently the ultimate regime, re-

mains challenging, both in experiments and numerical simulations. The highest achievable  $Ra$  in experiments is  $Ra \approx 10^{15}$  [6], and in three-dimensional numerical simulations is  $Ra \approx 10^{12}$  [8]. A challenge in experiments is non-Oberbeck–Boussinesq effects [6], i.e. the temperature variation of the fluid properties, and the main challenge in the numerical simulations is the computational cost [9], e.g. increasing  $Ra$  by 10 times at  $Pr = 0.7$  increases the CPU hours by about 24 times.

Studies have attempted to reach the ultimate regime in closely related flows, or by introducing a secondary effect to the Rayleigh–Bénard convection. These efforts include: 1) introducing shear [10], which induces an artificial wind to the flow; 2) investigating vertical natural convection which has a stronger wind than in Rayleigh–Bénard flow [11]; 3) performing two-dimensional numerical simulations of Rayleigh–Bénard convection [12]; or 4) considering a low-Prandtl-number Rayleigh–Bénard convection [13]. Here, we consider a centrifugal buoyancy driven convection as another approach to the ultimate regime. Unlike vertical natural convection, where the wind is set only by the Rayleigh number, in centrifugal convection the Rossby number enters as an additional control parameter to ‘tune’ the wind strength. And unlike sheared Rayleigh–Bénard convection, in which shear and buoyancy act as two separate driving mechanisms, in centrifugal convection buoyancy is the only driving mechanism; the Coriolis force simply reorganises the flow. In other words, there is no flow if  $Ra = 0$ .

### Flow setup

#### Governing Equations

We consider a fluid with density  $\rho$ , kinematic viscosity  $\nu$ , thermal conductivity  $\kappa$ , and thermal expansion coefficient  $\beta$ . The governing equations are derived from the incompressible Navier–Stokes equations governing the flow in a concentric cylindrical annulus with gap  $H$  (figure 1a) in the frame rotating in clockwise direction about its cylindrical axis  $\zeta$  at constant rotational speed  $\Omega$ , as described by velocity  $\mathbf{v} = v_r \mathbf{e}_r + v_\phi \mathbf{e}_\phi + v_\zeta \mathbf{e}_\zeta$ , and temperature  $T$  in cylindrical coordinates  $(r, \phi, \zeta)$ . The boundary conditions in this rotating frame are no-slip and impermeable walls,  $\mathbf{v}(r = R - H) = \mathbf{v}(r = R) = 0$ , corresponding to the inner and outer walls, respectively, and isothermal walls with the prescribed temperature difference  $\Delta T = T_H - T_L$ , with  $T(r = R - H) = T_L$  and  $T(r = R) = T_H$ , corresponding to an inner colder wall and an outer hotter wall. We have invoked the Oberbeck–Boussinesq approximation, which assumes constant fluid properties,  $\nu$ ,  $\kappa$  and  $\beta$ , and that density variations are only dynamically important in the buoyancy term. In the buoyancy term the density variation is  $(\rho - \rho_o) = -\beta \rho_o \theta$ , where  $\rho_o = \rho(T_o = (T_H + T_L)/2)$ , the reference density at temperature  $T_o$ , and  $\theta = T - T_o$ , the temperature variation relative to  $T_o$ . For the

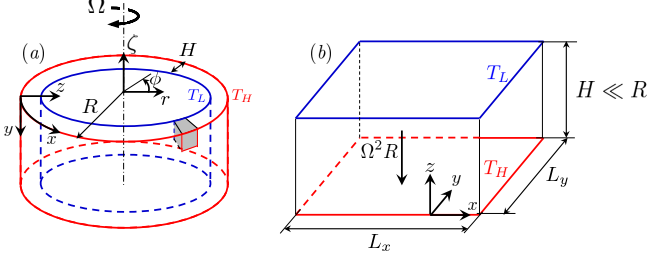


Figure 1: Setup of flow: (a) Centrifugal buoyancy-driven convection in concentric cylinder with gap  $H$  and outer cylinder radius  $R$ . The two cylinders undergo clockwise rotation about their axis  $\zeta$ , with rotational speed  $\Omega$ . Outer cylinder (—) is hotter than the inner cylinder (—); (b) the computational domain as a small chunk of the concentric cylinder, with  $H \ll R$ , (the grey cube in a), which is rectilinear, and  $L_x$  and  $L_y$  are the domain sizes in the streamwise (circumferential) and spanwise (axial) directions.

sake of brevity we refer the reader to [14] for the equations in the  $(r, \phi, \zeta)$  coordinate system. Since the equations are presented in a rotating frame, two additional terms appear in the Navier–Stokes equations: the Coriolis force  $-2\Omega v_\phi \mathbf{e}_r + 2\Omega v_r \mathbf{e}_\phi$ , and the centrifugal acceleration,  $-\beta\Omega^2 r \mathbf{e}_r$ .

To further simplify the problem, we consider the thin-shell limit,  $\varepsilon \equiv H/R \ll 1$  (figure 1b). To this end, we transform the equations from  $(r, \phi, \zeta)$  into curvilinear coordinates  $(x, y, z)$  with the origin placed at the outer cylinder. The transformed coordinates will be  $x = r\phi, y = -\zeta, z = R - r$ , and the transformed velocity will be  $u = v_\phi, v = -v_\zeta, w = -v_r$ . Then, we non-dimensionalise the variables using the gap width  $H$ , the free-fall velocity  $U \equiv (\Omega^2 R \beta \Delta T H)^{1/2}$ , and  $\Delta T$ :  $\tilde{x} = x/H, \tilde{y} = y/H, \tilde{z} = z/H, \tilde{t} = tU/H$  are the scaled space and time coordinates,  $\tilde{u} = u/U, \tilde{v} = v/U, \tilde{w} = w/U$  are the scaled velocity components, and  $\tilde{p} = (p - \rho_o \Omega^2 R^2/2)/(\rho_o U^2)$  and  $\tilde{\theta} = \theta/\Delta T$  are the scaled pressure and temperature variation. Substituting these into the transformed equation, and expanding in small  $\varepsilon$ , we obtain, to leading order:

$$\tilde{\nabla} \cdot \tilde{\mathbf{u}} = 0 \quad (1)$$

$$\partial_{\tilde{t}} \tilde{u} + \tilde{\mathbf{u}} \cdot \tilde{\nabla} \tilde{u} = -\partial_{\tilde{x}} \tilde{p} + (Ra/Pr)^{-1/2} \tilde{\nabla}^2 \tilde{u} - Ro^{-1} \tilde{w}, \quad (2)$$

$$\partial_{\tilde{t}} \tilde{v} + \tilde{\mathbf{u}} \cdot \tilde{\nabla} \tilde{v} = -\partial_{\tilde{y}} \tilde{p} + (Ra/Pr)^{-1/2} \tilde{\nabla}^2 \tilde{v}, \quad (3)$$

$$\partial_{\tilde{t}} \tilde{w} + \tilde{\mathbf{u}} \cdot \tilde{\nabla} \tilde{w} = -\partial_{\tilde{z}} \tilde{p} + (Ra/Pr)^{-1/2} \tilde{\nabla}^2 \tilde{w} + Ro^{-1} \tilde{u} + \tilde{\theta}, \quad (4)$$

$$\partial_{\tilde{t}} \tilde{\theta} + \tilde{\mathbf{u}} \cdot \tilde{\nabla} \tilde{\theta} = (RaPr)^{-1/2} \tilde{\nabla}^2 \tilde{\theta} \quad (5)$$

Since  $\tilde{x} = O(1)$  and  $\tilde{y} = O(1)$ , the thin shell limit implies  $x \ll R$  and  $y \ll R$ , i.e. the computational domain is a small chunk of the concentric cylinder (figure 1a, the grey cube). In this thin-shell limit (1)-(5) are identical to the Navier–Stokes equations in the Cartesian coordinate system. These equations reveal that this flow is characterised by three non-dimensional numbers: 1) Rayleigh number  $Ra \equiv (\Omega^2 R \beta \Delta T H^3)/(v\kappa)$ , 2) Rossby number  $Ro \equiv U/(2\Omega H) = (\beta \Delta T R/H)^{1/2}/2$ , and 3) Prandtl number  $Pr \equiv v/\kappa$ . Due to the choice of free-fall velocity  $U$  for scaling,  $Ro$  does not depend on  $\Omega$ . However, the terms  $-Ro^{-1} \tilde{w}$  and  $Ro^{-1} \tilde{u}$  on the right-hand side of equations (2) and (4) still represent the Coriolis effect. The results are presented in terms of  $(x, u)$ ,  $(z, w)$  and  $(y, v)$ , the circumferential, radial and axial directions of the cylindrical shell, respectively, and are noted as the streamwise, wall-normal and spanwise directions. The inner and outer walls of the cylindrical shell are also noted as the top and bottom walls, respectively.

| $Ra$      | $N^3$   | $(\Delta x/\eta)_{max}$ | $(\Delta y/\eta)_{max}$ | $(\Delta z/\eta)_{max}$ |
|-----------|---------|-------------------------|-------------------------|-------------------------|
| $10^7$    | $128^3$ | 1.9                     | 1.9                     | 1.3                     |
| $10^8$    | $256^3$ | 2.1                     | 2.1                     | 1.5                     |
| $10^9$    | $512^3$ | 2.1                     | 2.1                     | 1.6                     |
| $10^{10}$ | $512^3$ | 6.5                     | 6.5                     | 4.6                     |

Table 1: Summary of number of grid points  $N$  and resolution quality, based on the maximum ratio of the local grid size over the local Kolmogorov length-scale,  $\eta(z) = (v^3/\varepsilon)^{1/4}$ , where  $\varepsilon$ , the turbulent dissipation-rate, is averaged over time and in the  $xy$ -plane. For each  $Ra$ , six  $Ro^{-1}$  was attempted:  $Ro^{-1} = (0, 0.3, 0.5, 0.6, 0.8, 1.0)$ . For all cases  $Pr = 0.7$  and  $L_x/H \times L_y/H = 1 \times 1$ .

### Direct Numerical Simulation

Equations (1)-(5) were solved over a rectilinear box (figure 1b) with periodic boundary conditions imposed to the streamwise and spanwise directions. The top and bottom wall boundary conditions are  $\tilde{\mathbf{u}}(\tilde{z} = 0) = \tilde{\mathbf{u}}(\tilde{z} = 1) = 0, \tilde{\theta}(\tilde{z} = 0) = 1/2$  and  $\tilde{\theta}(\tilde{z} = 1) = -1/2$ . The equations are solved using a fully conservative fourth-order finite difference code, validated in the previous DNS studies of similar flow physics [11]. Table 1 lists all the simulation cases. For all cases  $Pr = 0.7, L_x/H \times L_y/H = 1 \times 1$ , and the same number of grid points,  $N$ , is used in the three directions. The grid points are uniformly distributed in the  $x$ - and  $y$ -directions, and are stretched in the  $z$ -direction following [9]. In total, four  $Ra$  were simulated, ranging from  $10^7$  to  $10^{10}$ , and at each  $Ra$ , the inverse Rossby number  $Ro^{-1}$  was varied from zero (no Coriolis force) to unity (large Coriolis force). The appropriateness of the grid resolutions are assessed in Table 1 which lists the grid sizes relative to the Kolmogorov length-scale  $\eta$ . Since  $\eta$  varies with  $z$ , the maximum ratio of local grid size compared to local  $\eta$ , which occurs at the walls, is reported. At all  $Ra$  the maximum grid spacing is  $2\eta$ , except at  $Ra = 10^{10}$ . However, grid convergence study at the lower  $Ra$  reveals that the difference between the grid spacing of  $6\eta$  and  $2\eta$ , in terms of the Nusselt number, mean and r.m.s. quantities is less than 4%.

### Results

The resulting Nusselt number  $Nu = (H/\Delta T)|d\tilde{\theta}/dz|_w$  and skin-friction coefficient  $C_f = 2\nu|d\tilde{u}/dz|_w/U^2$  are shown in figures 2 and 3, where  $|d\tilde{\theta}/dz|_w$  and  $|d\tilde{u}/dz|_w$  are the absolute wall-gradients of the temperature and velocity, averaged over time,  $xy$ -plane and both walls. In figure 2 when  $Ro^{-1} = 0$  (no Coriolis force),  $Nu$  follows the Grossman & Lohse theory (---). At a constant  $Ra$ , as  $Ro^{-1}$  increases (i.e. Coriolis force increases),  $Nu$  decreases until it reaches a minimum at the optimal  $Ro_{opt}^{-1}$ . Increasing  $Ro^{-1}$  beyond  $Ro_{opt}^{-1}$  leads to increase in  $Nu$  (except  $Ra = 10^7$ ). This is better shown in figure 3(a,b): at each  $Ra$ , there exists an  $Ro_{opt}^{-1}$  at which  $Nu$  is minimum and  $C_f$  is maximum. Considering the sensitivity of  $Ro_{opt}^{-1}$  with respect to  $Ra$  (figure 3), reveals that  $Ro_{opt}^{-1} \simeq 0.8$  for all values of  $Ra$ . In figure 2, if we fix  $Ro^{-1}$  at  $Ro_{opt}^{-1}$  (\*), and increase  $Ra$ , we observe that above  $Ra = 10^9$ , the  $Nu$  scaling steepens towards  $Ra^{0.38}$ , implying the flow transition towards the ultimate regime.

The mechanism behind the minimum  $Nu$  at  $Ro_{opt}^{-1}$  was explained by Chong *et al.* [15], through a unifying view on the interplay between a driving force (e.g. buoyancy), and a stabilising force (e.g. Coriolis force, salinity or confinement). As the stabilising force increases, at an intermediate regime it becomes strong enough that it organises the flow structures in the bulk, yet not too strong to suppress the turbulent flow motions. Chong *et*

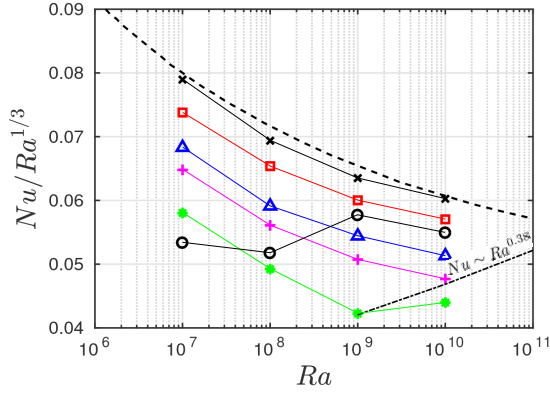


Figure 2:  $Nu/Ra^{1/3}$  for all cases listed in table 1.  $Nu = (H/\Delta T)|d\bar{\theta}/dz|_w$ , where  $\bar{\theta}$  is the averaged  $\theta$  over  $(x,y)$  plane and time, and  $|d\bar{\theta}/dz|_w = (|d\bar{\theta}/dz|_{z=0} + |d\bar{\theta}/dz|_{z=H})/2$ .  $Ro^{-1} = 0$  ( $\times$ ),  $Ro^{-1} = 0.3$  ( $\square$ ),  $Ro^{-1} = 0.5$  ( $\triangle$ ),  $Ro^{-1} = 0.6$  ( $+$ ),  $Ro^{-1} = 0.8$  ( $*$ ) and  $Ro^{-1} = 1.0$  ( $\circ$ ). Grossmann & Lohse theory [4] (---);  $Nu$  scaling by  $Ra^{0.38}$  (—).

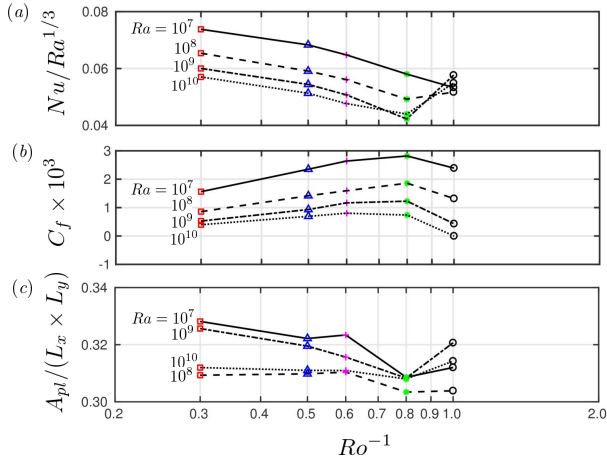


Figure 3: Variation of (a)  $Nu/Ra^{1/3}$ , (b)  $C_f$  and (c)  $A_{pl}$  cold plume coverage at the edge of the bottom wall boundary layer, versus  $Ro^{-1}$  at different  $Ra$ .  $C_f = 2\nu|d\bar{u}/dz|_w/U^2$ , where  $\bar{u}$  is the averaged  $u$  over  $(x,y)$  plane and time, and  $|d\bar{u}/dz|_w = (|d\bar{u}/dz|_{z=0} + |d\bar{u}/dz|_{z=H})/2$ .  $Ra = 10^7$  (—),  $Ra = 10^8$  (---),  $Ra = 10^9$  (-·-·-),  $Ra = 10^{10}$  (·····). Each symbol corresponds to one  $Ro^{-1}$  consistent with figure 2.

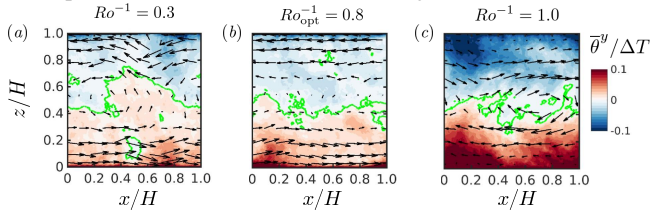


Figure 4: Instantaneous spanwise averaged velocity vector  $(\bar{u}^y, \bar{w}^y)$ , overlaid by the instantaneous spanwise-averaged temperature field  $(\bar{\theta}^y)$  at  $Ra = 10^{10}$ , and different  $Ro^{-1}$ . (a)  $Ro^{-1} = 0.3$ , (b)  $Ro^{-1} = 0.8$  and (c)  $Ro^{-1} = 1.0$ . The green line locates  $\bar{\theta}^y = 0$ .

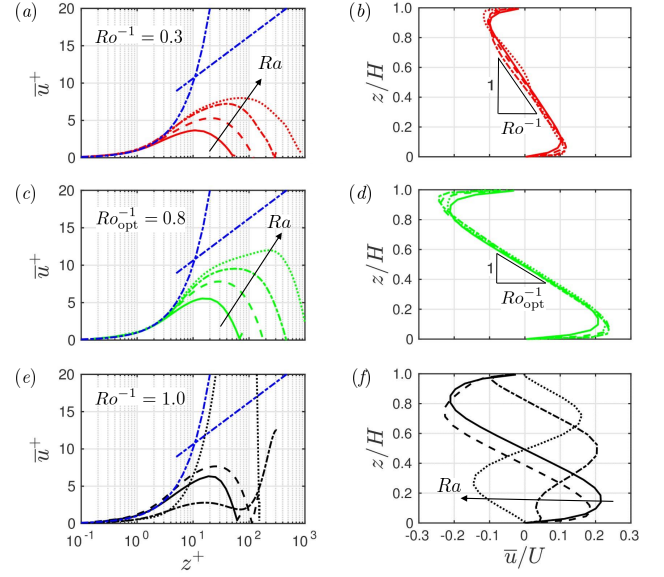


Figure 5: Profiles of  $\bar{u}$  at (a,b)  $Ro^{-1} = 0.3$ , (c,d)  $Ro^{-1} = 0.8$  and (e,f)  $Ro^{-1} = 1.0$ . The arrows show the directions of increase in  $Ra$ . (a,c,e)  $\bar{u}^+ = \bar{u}/u_\tau$  versus  $z^+ = zU/\nu$ ; (b,d,f)  $\bar{u}/U$  versus  $z/H$ .  $u_\tau = (\nu|d\bar{u}/dz|_{z=0})^{1/2}$ .  $Ra = 10^7$  (—),  $Ra = 10^8$  (---),  $Ra = 10^9$  (-·-·-),  $Ra = 10^{10}$  (·····). The lines (—·—) in (a,c,e) are:  $\bar{u}^+ = z^+$  and  $\bar{u}^+ = 1/0.41 \ln(z^+) + 5.2$  [16]. The right triangle in (b,d) shows the slope  $(H/U)(d\bar{u}/dz) \simeq -Ro^{-1}$ .

*al.*[15] explained the role of stabilising force in forming highly coherent plume-like structures that preserve their heat against thermal or molecular diffusion. However, the fundamental difference between our setup and [15] is in the axis of rotation and the resulting coherent structures. In [15] axis of rotation was in the wall-normal direction, and the Coriolis force was acting in the  $x$ - and  $y$ -directions. The resulting coherent structures, at  $Ro_{opt}^{-1}$ , were appearing as circular columns oriented aligned with the axis of rotation ( $z$ ), which were maximising the heat transfer (maximum  $Nu$ ), between the the top and bottom walls. Here, axis of rotation is in the  $y$ -direction, and the Coriolis force is acting in the  $x$ - and  $z$ -directions. The result of the increase in the stabilising force, at  $Ro_{opt}^{-1}$  (figure 4b), is a bidirectional wind that drives the hot and cold fluid in the positive and negative  $x$ -direction, below and above the domain centreline, respectively. Consequently, the wind inhibits the heat transfer between the end walls, leading to the minimum  $Nu$ . To better quantify the morphological behaviour of the wind, following [15] in figure 3(c) we plot the area ratio  $A_{pl}/(L_x \times L_y)$  covered by the cold fluid at the edge of the bottom thermal boundary layer ([15], supplemental material). It is seen that at a certain level of stabilising force ( $Ro_{opt}^{-1}$ ) smaller portion of the cold fluid covers the bottom thermal boundary layer compared to the weaker stabilising forces ( $Ro^{-1} < Ro_{opt}^{-1}$ ). It is also seen that beyond  $Ro_{opt}^{-1}$  ( $Ro^{-1} = 1.0$ ), the stronger stabilising force increases the cold fluid coverage of the bottom thermal boundary layer, coincident with the increasing  $Nu$ . At  $Ro^{-1} = 1.0$  the wind is weakened, and the hot and cold fluids penetrate deeper to the bulk of the flow (figure 4c).

The wind strength is demonstrated in the mean velocity profiles in figure 5. In each figure,  $Ro^{-1}$  is fixed and  $Ra$  is increased, and each row shows one  $Ro$ . Comparing the profiles between  $Ro^{-1} = 0.3$  (figure 5a,b),  $Ro^{-1} = 0.8$  (figure 5c,d), and  $Ro^{-1} = 1.0$  (figure 5e,f), the maximum wind velocity is attained at  $Ro_{opt}^{-1} = 0.8$ . At  $Ro_{opt}^{-1} = 0.8$ , as  $Ra$  increases, the profiles trend

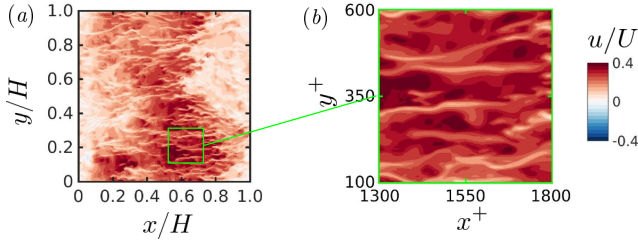


Figure 6: Near-wall instantaneous  $u$  at  $z^+ = zu\tau/\nu = 15$ ,  $Ra = 10^{10}$  and  $Ro_{\text{opt}}^{-1} = 0.8$ . (b) shows the magnified green framed square in (a) which encloses an area of  $500 \times 500$  wall units.

towards the Prandtl-von Kármán (logarithmic) behaviour (---), however, full collapse on the logarithmic law is still not reached at  $Ra = 10^{10}$ . Considering figure 5(b,d) for  $Ro^{-1} \leq Ro_{\text{opt}}^{-1}$ , the mean profiles in the core of the domain ( $0.3 \lesssim z/H \lesssim 0.7$ ), yield the slope  $(H/U)(d\bar{u}/dz) \simeq -Ro^{-1}$ . This approximation can be derived by plane and time averaging equations (1) and (2), and combining them together. At  $Ro^{-1} = 1.0 > Ro_{\text{opt}}^{-1}$ , the wind is weakened and its direction oscillates. For  $Ro^{-1} \gg 1.0$  (not shown), the bidirectional wind is transformed into a field of 2D vortices in the  $xz$ -plane. At that point the momentum balance is only between the Coriolis force, buoyancy and pressure gradient. This flow regime, is related to the geostrophic regime in the planetary flows [14].

The maximum wind speed at  $Ro_{\text{opt}}^{-1} = 0.8$ , at sufficiently high  $Ra$ , modifies the near-wall structures to those seen in wall-bounded flows (figure 5). The instantaneous field of  $u$  at  $z^+ = 15$ ,  $Ro_{\text{opt}}^{-1} = 0.8$  and  $Ra = 10^{10}$  yields the emergence of the near-wall streaks, another indication of the flow tendency towards the ultimate regime. The green square, magnified in figure 5(b), highlights the approximately 100 wall units spacing between the near-wall streaks.

## Conclusions

We performed DNS of centrifugal buoyancy-driven convection approaching but not reaching the ultimate regime of thermal convection. To this aim, a cylindrical shell was considered, with a cold inner wall and a hot outer wall, rotating about its axis at constant angular velocity. Three non-dimensional numbers characterise the flow: Prandtl number  $Pr$ , Rayleigh number  $Ra$ , and Rossby number  $Ro$ .  $Pr = 0.7$ , corresponding to air was considered. Thus,  $Ra$  and  $Ro$  were the remaining control parameters;  $Ra$  characterises the buoyancy force, and  $Ro$  characterises the Coriolis force (i.e. higher  $Ro^{-1}$ , higher Coriolis force). Similar to Chong *et al.* [15], the flow is subjected to an interplay between the driving buoyancy force and the stabilising Coriolis force. However, at the optimal condition, owing to the different axis of rotation, rather than the coherent plume-like structures, seen in [15] that maximised heat transport, a strong bidirectional wind is formed (at  $Ro_{\text{opt}}^{-1} \simeq 0.8$ ) that minimises heat transport. By increasing  $Ra$ , at  $Ro_{\text{opt}}^{-1}$ , the mean flow approaches Prandtl-von Kármán (logarithmic) behaviour, yet full collapse on the logarithmic law is not reached at  $Ra = 10^{10}$ .

## Acknowledgements

This research was supported by resources provided by The Pawsey Supercomputing Centre with funding from the Australian Government and the Government of Western Australia and by the National Computing Infrastructure (NCI), which is supported by the Australian Government. The support of the Australian Research Council is also gratefully acknowledged.

## References

- [1] Ahlers, G., Grossmann, S. and Lohse, D., Heat transfer and large scale dynamics in turbulent Rayleigh-Bénard convection, *Rev. modern physics*, **81**, 2009, 503.
- [2] Lohse, D. and Xia, K. Q., Small-scale properties of turbulent Rayleigh-Bénard convection, *Ann. Rev. Fluid Mech.*, **42**, 2010.
- [3] Kraichnan, R. H., Turbulent thermal convection at arbitrary Prandtl number, *Phys. Fluids*, **5**, 1962, 1347–1389.
- [4] Grossmann, S. and Lohse, D., Scaling in thermal convection: a unifying theory, *J. Fluid Mech.*, **407**, 2000, 27–56.
- [5] He, X., Funfschilling, D., Bodenschatz, E. and Ahlers, G., Heat transport by turbulent Rayleigh-Bénard convection for  $Pr \approx 0.8$  and  $4 \times 10^{11} \leq Ra \leq 2 \times 10^{14}$ : ultimate-state transition for aspect ratio  $\Gamma = 1.00$ , *New J. Phys.*, **14**, 2012, 063030.
- [6] Ahlers, G., He, X., Funfschilling, D. and Bodenschatz, E., G., Heat transport by turbulent Rayleigh-Bénard convection for  $Pr \approx 0.8$  and  $3 \times 10^{12} \leq Ra \leq 10^{15}$ : aspect ratio  $\Gamma = 0.50$ , *New J. Phys.*, **14**, 2012, 103012.
- [7] Grossmann, S. and Lohse, D., Multiple scaling in the ultimate regime of thermal convection, *Phys. Fluids*, **23**, 2011, 045108.
- [8] Stevens, R. J., Lohse, D. and Verzicco, R., Prandtl and Rayleigh number dependence of heat transport in high Rayleigh number thermal convection, *J. Fluid Mech.*, **688**, 2011, 31–43.
- [9] Shishkina, O., Stevens, R. J. A. M., Grossmann, S. and Lohse, D., Boundary layer structure in turbulent thermal convection and its consequences for the required numerical resolution, *New J. Phys.*, **12**, 2010, 075022.
- [10] Blass, A., Zhu, X., Favre, J., Verzicco, R., Lohse, D., Stevens, R. J. A. M. (personal communication).
- [11] Ng, C. S., Ooi, A., Lohse, D. and Chung, D., Changes in the boundary-layer structure at the edge of the ultimate regime in vertical natural convection, *J. Fluid Mech.*, **825**, 2017, 550–572.
- [12] Zhu, X., Varghese, M., Stevens, R. J. A. M., Verzicco, R. and Lohse, D., Transition to the ultimate regime in two-dimensional Rayleigh-Bénard convection, *Phys. Rev. Lett.*, **120**, 2018, 144502.
- [13] Schumacher, J., Bandaru, V., Pandey, A and Scheel, J. D., Transitional boundary layers in low-Prandtl-number convection, *Phys. Rev. Fluids*, **1**, 2016, 084402.
- [14] Kundu, P. K. and Cohen, L. M, *Fluid mechanics*, Academic Calif., 1990.
- [15] Chong, K. L., Yang, Y., Huang, S. D., Zhong, J. Q., Stevens, R. J., Verzicco, R., Lohse, D. and Xia, K. Q., Confined Rayleigh-Bénard, Rotating Rayleigh-Bénard, and Double Diffusive Convection: A unifying view on turbulent transport enhancement through coherent structure manipulation. *Phys. Rev. Lett.*, **119**, 2017, 064501.
- [16] Yaglom, A. M., Similarity laws for constant-pressure and pressure-gradient turbulent wall flows, *Ann. Rev. Fluid Mech.*, **11**, 1979, 505–540.